Journal of Manufacturing Processes 38 (2019) 49–62

Contents lists available at ScienceDirect

Journal of Manufacturing Processes

journal homepage: www.elsevier.com/locate/manpro

Technical Paper

Accounting Bauschinger effect in the numerical simulation of constrained groove pressing process

Sunil Kumar[a], Krishnaswamy Hariharan[b,*], Ravi Kumar Digavalli[a], Surajit Kumar Paul[c]

[a] Department of Mechanical Engineering, Indian Institute of Technology Delhi, New Delhi 110016, India
[b] Department of Mechanical Engineering, Indian Institute of Technology Madras, Chennai 600036, India
[c] Department of Mechanical Engineering, Indian Institute of Technology Patna, Patna 801106, India

ARTICLE INFO

Keywords:
Severe plastic deformation
Constrained groove pressing
Kinematic hardening
Chaboche model

ABSTRACT

Constrained groove pressing (CGP) is one of the severe plastic deformation techniques to achieve ultrafine grains in bulk sheet metals. The CGP process induces large plastic strain through incremental steps of shear and reverse shear using grooved and flat dies. The equivalent plastic strain distribution during CGP process can be correlated to the extent of grain refinement and the uniformity of ultrafine grains. The numerical analysis in the past have assumed isotropic hardening to model CGP process that does not consider the Bauschinger effect due to continuous change in deformation path between subsequent stages. In the present work, the effect of Bauschinger effect is considered using a combined isotropic-kinematic hardening model in simulation. The finite element model assuming isotropic hardening is validated with the results available in literature. Experiments on CGP were performed using three different materials and were modelled using both isotropic and combined hardening models. The maximum strain and the strain inhomogeneity predicted using combined hardening models were consistently greater than the isotropic hardening assumption.

1. Introduction

Severe plastic deformation (SPD) processes are used to produce bulk ultrafine grained structure with special properties such as high strength and toughness, corrosion resistance, high fatigue strength etc., as summarized in [1]. In SPD processes, material is subjected to intense plastic strain to achieve ultrafine grains in the order of sub-micron range. There are many established SPD techniques such as Equal channel angular pressing (ECAP) [2,3], High pressure torsion (HPT) [4], Repetitive corrugation and straightening (RCS) [5], Multi axial forging (MAF) [6], Asymmetric rolling (ASR) [7], Accumulative roll-bonding (ARB) [8], Twist extrusion (TE) [9] and Constrained groove pressing (CGP) [10] to name a few. Among these, RCS, ASR, ARB and CGP methods are suitable for sheet metal applications.

In CGP process, the material is subjected to repeated shear deformation by subsequent pressing between asymmetric grooved and flat dies. Dies are made in such a way that material is constrained along its periphery to avoid any process induced dimensional change. The material is subjected to repeated passes till failure, each pass consists of four stages: two grooving operations alternating with two flattening operations, as schematically illustrated in Fig. 1. Shin et al. [10] showed that at the end of each pass, the entire material is subjected to an effective plastic strain increment of 1.16. There are distinct advantages of CGP over the other techniques such as: no dimensional change in processed sheet, large strain imposed in single pass, easy handling and fabrication of dies and simple experimental setup.

Improved mechanical properties through CGP has been accomplished in a wide range of materials with different crystal structures such as BCC (low carbon steel investigated by [11]), FCC (aluminium by [12,13]) and HCP (titanium by [14,15]) and multiphase alloys such as Cu-38 Zn alloys [16]. Along with dislocation interaction, other grain boundary effects such as diffusion and grain boundary sliding occurs resulting in increased toughness [17]. In general, the strength increases whereas the rate of strain hardening and ductility decrease with the increase in number of passes. Humphreys and Hatherly [18] observed that after certain number of passes, the strength decreases due to dislocation annihilation by dynamic recovery. Better correlation with experimental results was found [19,20] when modelling the CGP process with dislocation density model, suggesting the validity of dislocation strengthening mechanism. Further increase in plastic strain through the number of passes leads to failure by cracking [16]. Attempts have been made in the past to increase the grain refinement during CGP by

* Corresponding author.
E-mail addresses: sunil30111988@gmail.com (S. Kumar), hariharan@iitm.ac.in (H. Krishnaswamy), dravi@mech.iitd.ac.in (R.K. Digavalli), surajit@iitp.ac.in (S.K. Paul).

https://doi.org/10.1016/j.jmapro.2018.12.013
Received 12 April 2018; Received in revised form 24 November 2018; Accepted 11 December 2018

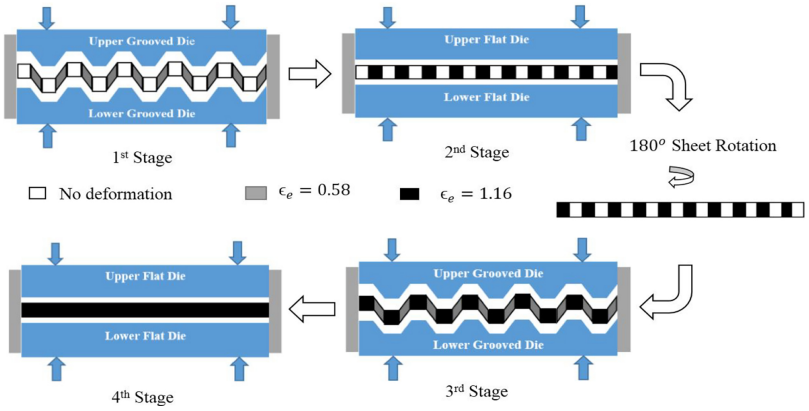

Fig. 1. Schematic diagram of constrained groove pressing (CGP) process.

postponing the fracture. Krishnaiah et al. [21,22] tried to suppress the dynamic recovery of dislocations by subjecting the material to cryogenic treatments, though no improvements was observed. Sajadi et al. [23] used two additional thinner sheets above and below the deforming sheet during CGP to reduce the surface cracking and to improve uniform strain distribution through the thickness. Wang et al. [24] showed that lubrication reduce the surface residual stress in CGP. These studies demonstrate that friction between the die and the deforming sheet plays an important role in the maximum strain that can be imparted during CGP. Increased friction introduces non homogenous strain through the thickness resulting in reduced maximum strain. Peng et al. [16,25] reported that wider groove area in CGP reduced the risk of cracking in Cu-Zn alloys. This improved the strain uniformity in CGP process.

Through CGP process, efforts have been made to successfully increase the strength of the materials for various industrial applications (refer [26]). The degree of grain refinement is closely related to the effective plastic strain, evident from the increase in strength with the number of passes. In addition to the effective strain, it is also noted that homogenous strain distribution is important to avoid premature failure by localized necking. Homogenous strain distribution during CGP gains importance in related applications. For instance, SPD processed UFG materials find applications related to microforming small components [27], where homogenous grain distribution has a significant role in better formability and accuracy [28]. It was observed [29] that regions under and close to center in slant sections of CGP produce more grain refinement than the corners as the latter is influenced by additional bending around the radius. Understanding the plastic strain distribution during the SPD process is essential to optimize the process outcome for specific applications.

Researchers have used numerical techniques to simulate the deformation behavior and strain distribution during CGP. Yoon et al. [20] showed that the non uniform strain distribution in transverse direction is due to lesser shear deformation at the interface of slant and flat regions. Satheesh Kumar et al. [30] investigated deformation behaviour of aluminum in CGP process and validated the results with hardness distribution. Inhomogeneous strain distribution was observed throughout the sheet. The middle surface is subjected to superior strain distribution compared to top and bottom surface after one pass. Wang et al. [31] analysed the plastic strain distribution and correlated it with the geometry of the CGP die.

Most of the numerical analysis discussed above simulate only the first stage of the process and not the entire four stages constituting a pass. The work hardening in CGP involves strain path reversal in each successive stage. Work hardening of the material is different for forward shear deformation of first and third stage compared to reverse shear deformation of second and fourth stages. This reversal of plastic shear strain deformation exhibit Bauschinger effect and softening of material [32–35] and is observed in severe plastic deformation [36,37]. Bauschinger effect is characterized by the softening of material with change in strain path. The Orowan mechanism was found to be the primary governing mechanism for the softening whereas the backstress and intergranular residual stresses aids the Orowan mechanism [38]. Using neutron diffraction experiments [39], the Bauschinger effect in pearlitic steel is correlated with the evolution of internal stress due to misfit strain between the ferrite and cementite phases. Similarly, the possibility of stress induced separation of partial dislocations in TWIP steels to induce Bauschinger effect has been investigated [40]. Hu et al. [41] developed a physically based self consistent crystal plasticity model to verify the influence of residual stress at different length scales on the Bauschinger effect.

While the underlying mechanism involves micro structural investigation across different material length scales, macroscopic models have been developed to predict the mechanical behaviour involving change in strain path. Bauschinger effect can be accounted phenomenologically using combined isotropic-kinematic hardening models that generalizes Prager's linear kinematic hardening model [42]. The kinematic hardening component is accounted in these models by the translation of yield surface. The non-linear kinematic hardening model proposed by Chaboche [43] is widely used. Several modifications of the model has been attempted to include permanent softening [44] and the effect of temperature [45], strain [46] and plastic anisotropy [47] on its parameters. Alternately, the asymmetry in yield surface due to Bauschinger effect can also be modelled using anisotropic hardening or distortion hardening approach [48]. Two surface models with a bounded second yield surface to model the kinematic component has been developed in the past [49]. Many new models have been proposed recently using the two yield surface approach [50–52]. The single surface models after Chaboche are computationally less expensive and are often preferred over two surface models [47].

The aim of present work is to develop a methodology to accurately simulate the mechanical behavior of material during CGP process that can assist in understanding the evolution and inhomogeneity in plastic strain distribution. Initially finite element simulations are performed following isotropic hardening assumption and compared with the results reported in literature. This was used to validate the finite element model and eliminate other errors in boundary conditions. Later, numerical studies were performed using combined isotropic-kinematic hardening models that account for the Bauschinger effect during strain reversal in higher stages. Physical experiments were performed using three different materials namely low carbon steel, commercially pure aluminum and aluminum alloy (AA5083). The experimental results were compared with the numerical predictions. It is shown that it is

Table 1
Chemical composition of low carbon steel, commercial aluminum and AA5083 alloy.

Low carbon steel							
Element	Fe	C	Mn	P	S	Al	Si
wt%	99.615	0.038	0.224	0.011	< 0.008	0.042	< 0.07
Commercial aluminum							
Element	Al	Cu	Mn	Mg	Fe	Zn	Si
wt%	97.96	0.147	0.438	0.256	0.82	0.042	0.225
Aluminum alloy (AA5083)							
Element	Al	Mg	Mn	Cr	Cu	Fe	Si
wt%	94.062	4.8	0.63	0.064	0.033	0.087	< 0.087

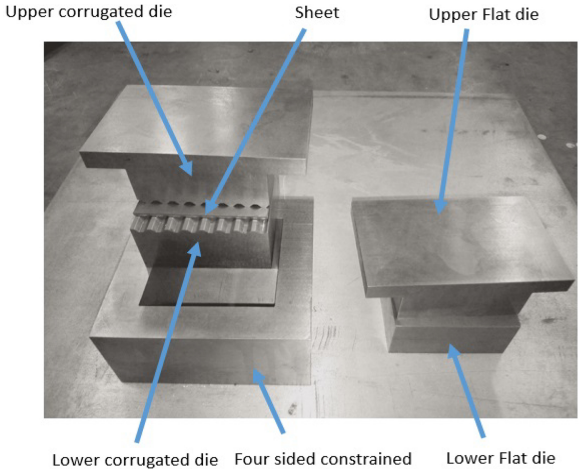

Fig. 2. Constrained groove pressing dies with sheet.

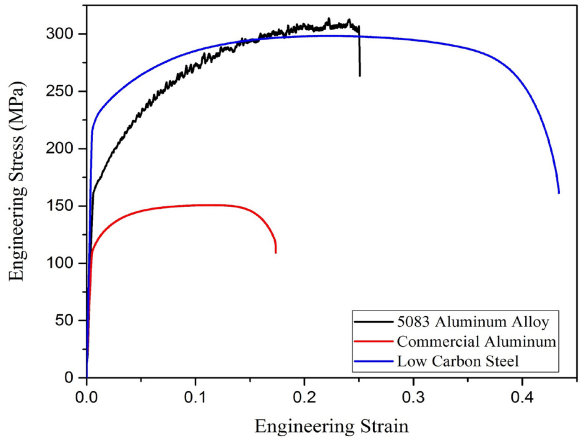

Fig. 3. Engineering stress–strain curves of the three as-received materials (initial strain rate = 0.001 s^{-1}).

important to simulate more than two stages of CGP as the mechanical behavior in higher stages were distinctly different from that of lower stages. In addition to that, simulating the process using combined hardening models provided more meaningful insight of the CGP process.

2. Experimental study

The chemical composition of the investigated materials, low carbon steel, commercially pure aluminum and aluminum alloy (AA5083) with fully annealed condition is shown in Table 1. Low carbon steel and commercial aluminum materials were selected for this process because they have relatively low strength with less alloying elements. AA5083 which is an Al-Mg alloy was investigated to understand the influence of alloying elements in the CGP process. All the sheets were of 2 mm thickness.

Uniaxial tensile tests as per ASTM-E8M [53] was performed in the as-received condition and at the end of each successive CGP pass. The die impressions post CGP process were removed physically prior to tensile test. All the tests were carried out in 100 kN INSTRON tensile testing machine with initial strain rate of 0.001 s^{-1}. The tests were repeated at least three times for repeatability. Cyclic tests with 1% constant strain amplitude were conducted on selected three materials (low carbon steel, commercial aluminum and AA5083) to evaluate the isotropic and kinematic hardening parameters. Specimens taken along rolling direction for cyclic tests are of 7.9 mm gauge length and 2 mm width in according to ASTM E606-92 [54] standard. 5 mm gauge length clip-on extensometer was attached to the specimen to measure the strains at constant strain rate of 0.02 s^{-1}. 50 cycles were recorded for each cyclic test. The material parameters for isotropic and kinematic hardening are determined by curve fitting the experimental response.

Vickers microhardness tests were carried out on commercial aluminum and low carbon steel in transverse and through thickness direction to estimate the non-uniformity in properties. A load of 100 g was applied for a dwelling time of 15 s at close distance for two consecutive reading. Hardness data was collected from nine locations in the transverse direction and four locations in through thickness direction after each pass. Inhomogeneity factor and dislocation density in the material was evaluated from the measured micro hardness values.

The CGP dies included lower grooved die, upper grooved die, lower flat die, upper flat die and constrained housing (for constraining sheet to avoid shape and size change and allowing upper and lower die to be aligned) and were designed for sheets with dimensions 64 mm × 64 mm × 2 mm as illustrated in Fig. 2. These dies were fabricated with 45° groove angle for 2 mm sheet thickness and this thickness is equivalent to width and depth of slant regions. During this process, molybdenum disulfide (MoS_2) was employed between die and sheet surfaces to reduce friction. All the experiments were carried out in a 100 t capacity double action hydraulic press at a velocity of 20 mm/s with a groove depth of 2 mm.

3. Finite element simulation with isotropic and combined hardening

Finite element simulation of the entire first pass involving four stages was carried out using commercially available ABAQUS software to understand the Bauschinger effect in CGP. Owing to symmetry, only a section of the deforming material (dimension 26 mm × 2 mm) under plane strain condition was considered for simulation. Around 1300 elements of element type CPE4R (bilinear plane strain quadrilateral, reduced integration, hourglass control) were used to model the deformable sheet. The tools were modelled as analytically rigid. The coefficient of friction between sheet and dies surfaces was assumed to

Table 2
Material properties incorporated in FE simulation in three chosen materials.

Material	Yield strength (MPa)	Ultimate strength (MPa)	Strain hardening exponent, *n*	Strength coefficient, *K* (MPa)
Low carbon steel	225	300	0.25	540
Commercial aluminum	116	148	0.18	250
AA5083	165	305	0.33	640

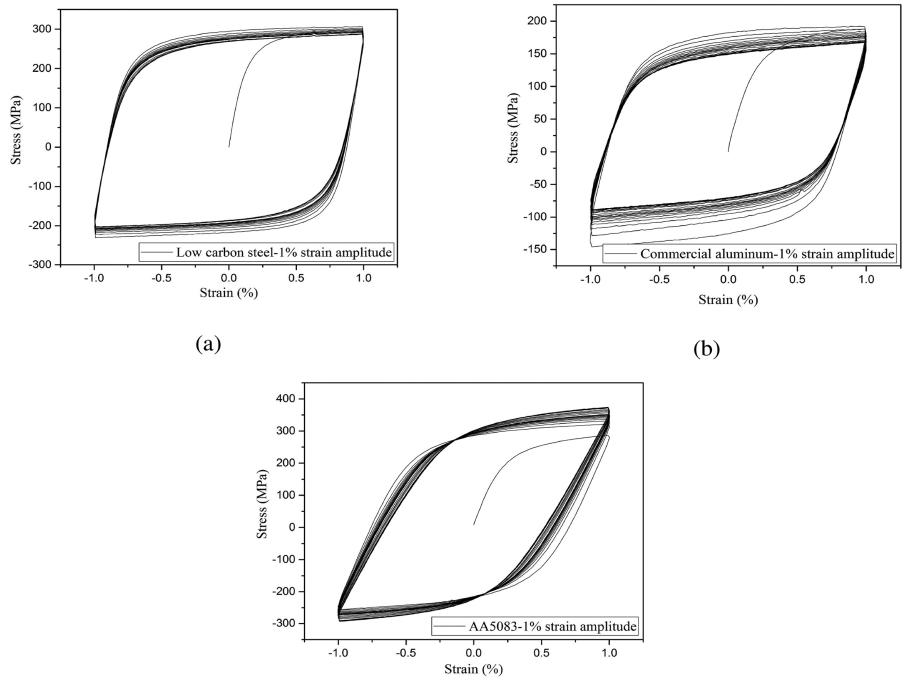

Fig. 4. Stress–strain cyclic curve with 1% constant strain amplitude of (a) low carbon steel, (b) commercial aluminum and (c) AA5083.

Table 3
Calibrated isotropic and kinematic hardening parameters for three materials.

Material	σ_y (MPa)	Q (MPa)	b	C_1 (MPa)	γ_1	C_2 (MPa)	γ_2	C_3 (MPa)	γ_3
Low carbon steel	225	−33.6	4.6	180,000	6000	30,000	500	1700	0
Commercial aluminum	116	−25.3	4.9	78,000	6000	156,000	600	1920	0
AA5083	165	38.0	2.8	318,000	4000	16,000	700	5000	0

be 0.1, as in literature, for e.g. [20,31]. Rate independent plastic deformation is assumed in the analysis. Displacement based constraints were used to define the tool motion. Springback simulation is carried out between subsequent stages to account for the redistribution of residual stresses.

Finite element simulations were performed using both isotropic and combined isotropic-kinematic hardening assumptions. The widely used Chaboche non-linear kinematic hardening model (NLK model) was utilized for the latter purpose. The Chaboche NLK model can be described as follows.

A combined isotropic- kinematic hardening yield criteria can be generally represented as Eq. (1)

$$F(\sigma, \epsilon_p) = |\sigma_{\text{eff}} - x| - \sigma_y = 0 \tag{1}$$

where F is the yield function of stress components (σ) and equivalent plastic strain (ϵ_p), σ_{eff} is effective yield stress, x is translational stress or backstress and σ_y is initial yield stress.

The backstress, x in the above equation offsets the yield surface in the principal stress space in the direction of effective plastic strain increment. In the case of proportional loading, evolution of back stress, x can be ignored. The strain hardening behavior is isotropic in nature and can be expressed purely by the yield locus size given by σ_y:

$$\sigma_y(\epsilon_p) = \sigma_o + R(\epsilon_p) \tag{2}$$

σ_o is the initial yield stress in the sheet used and $R(\epsilon_p)$ is the isotropic strain hardening function.

Hollomon hardening behavior expressing $R(\epsilon_p) = K\epsilon^n$ is found to model the behavior of wide range of materials. Voce hardening model represents another class of behavior where the stress saturates to a maximum critical value and is given by $R(\epsilon_p) = K(1 - e^{-b\epsilon})$.

In the case of combined isotropic-kinematic hardening models, the evolution of yield locus is modelled as a combination of isotropic component for expansion of yield locus followed by kinematic component for translation of the yield locus. The cyclic hardening behavior saturates to a stable hysteresis loop, during which the isotropic component ceases to operate and the stable hystereis loop is modelled by the kinematic component. Isotropic hardening model is introduced to incorporate cyclic softening effect, while kinematic hardening model simulate a stable stress–strain hysteresis loop. Therefore a saturating isotropic model of voce type was adopted in Chaboches NLK model, given by Eq. (4),

$$\dot{R} = b(Q - R)\dot{\epsilon_p}, \tag{3}$$

$$R(\epsilon_p) = Q(1 - e^{-b\epsilon_p}) \tag{4}$$

where Q and b are material constants. Q is the saturated value of $R(\epsilon_p)$ and b is the rate at which this saturation is achieved.

Like isotropic component, the evolution of back stress can also be modelled as a function of plastic strain, as in Armstrong and Frederick model [55] by Eq. (6),

$$\dot{x} = C\dot{\epsilon_p} - \gamma x\dot{p}, \tag{5}$$

$$x(\epsilon_p) = \frac{C}{\gamma}(1 - e^{-\gamma\epsilon_p}) \tag{6}$$

where C and γ are material constants and p is accumulative plastic strain.

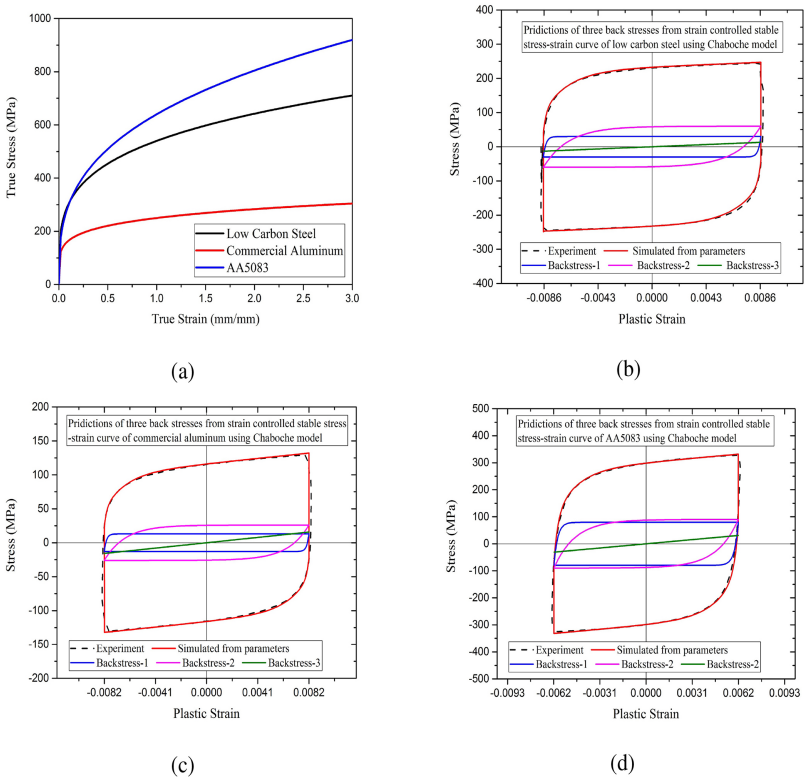

Fig. 5. (a) True stress–strain curve of three materials and comparison of cyclic stress–strain test and simulation from parameters: (b) low carbon steel, (c) commercial aluminum and (d) AA5083.

Chaboche [43] generalized the above by decomposing the back stress into three components for initial, transient and constant hardening behaviour, as given in Eq. (7).

$$x = \sum_{k=1}^{3} x_k, \tag{7}$$

where $x_k = \frac{C_k}{\gamma_k}(1 - e^{-\gamma_k \epsilon_p})$, k = 1–3 defines the individual back stress.

Chaboche's NLK model and its variants are widely used to simulate a variety of mechanical behavior involving strain path changes. Other successful approaches include multi-surface model and anisotropic hardening models. In the present work, Bauschinger effect is modelled using Chaboche NLK model. Estimated isotropic and kinematic hardening parameters from cyclic data are incorporated as input in FE simulation to consider the effect of non-linear isotropic and kinematic hardening in CGP process. The material parameters for the simulation are obtained from experimental test data obtained of stabilized strain-controlled cycles.

4. Results and discussion

The experimental results of tensile tests and cyclic tests are used to identify the Chaboche model parameters which were subsequently used to validate the experimental results of CGP using the investigated materials.

4.1. Mechanical characterization of initial material

The stress–strain curve obtained from monotonic tensile tests performed using all the three materials is shown in Fig. 3. The experimental results were fit using Swift law hardening model ($\sigma = K(\epsilon_o + \epsilon_p)^n$) and are tabulated below (Table 2). The parameters were used to model the isotropic hardening behaviour during CGP.

The monotonic stress–strain curve shown in Fig. 3 comprises isotropic and kinematic components of hardening. When a material pre-strained in one direction is reverse loaded, the softening can be modelled as backstress. The symmetric portion in a single cyclic curve indicates the isotropic component and the asymmetric component is twice the backstress. The cyclic stress–strain data for the first 50 cycles at 1% cyclic strain is shown in Fig. 4. The symmetric isotropic curve can be obtained by removing the back stress from each cycle and is fit using an exponential relation, $R = Q(1 - e^{-b\epsilon})$.

According to Chaboche model, kinematic hardening is decomposed linearly into three backstress components indicating initial softening, transient hardening and permanent softening. Each of these back stress components follow the exponential dependence with plastic strain, after Eq. (6). The material constants were identified by curve fitting the experimental data, adapting the procedure detailed in [56] and tabulated in Table 3. The identified constants were able to fit the experimental cyclic data very well, as shown in Fig. 5.

4.2. Experimental results on CGP

During CGP experiments, low carbon steel and commercially pure aluminium endured five (Fig. 6(a)) and three passes (Fig. 6(b)) respectively following which is failed by fracture. Surface cracks were observed in penultimate stages of both low carbon steel and commercially pure aluminium. The experiments using AA5083 failed before completing the first pass (Fig. 6(c)). Therefore AA5083 is not utilized for further discussion on experimental results. In all the cases, the surface cracks originate at the corner regions due to large local plastic strain and propagate parallel to groove orientation in subsequent stages (Fig. 6(d)). The size of the cracks in low carbon steel after third, fourth and fifth pass is 35 μm, 68 μm and 188 μm respectively. Similarly the cracks in commercial aluminum are 30 μm and 52 μm after second and third pass respectively. The magnified images of surface cracks of last pass of each material are shown in the actual image of the processed sheet as shown in the Fig. 6(a)–(c).

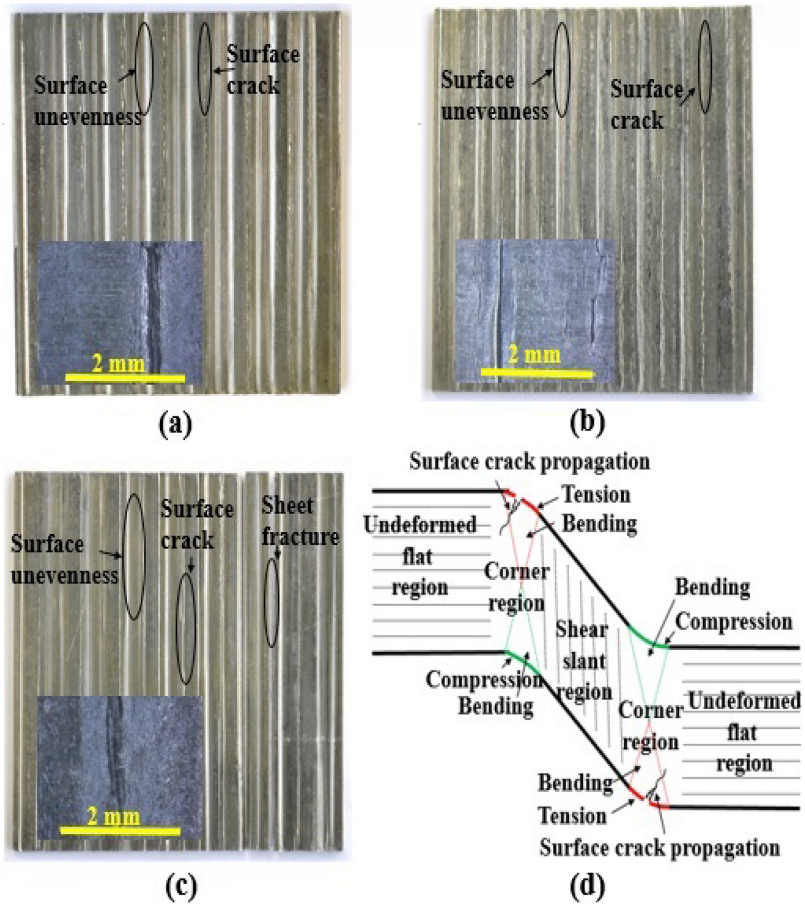

Fig. 6. CGP processed sheets (a) of low carbon steel after fifth pass, (b) of commercial aluminum after third pass, (c) of AA5083 after first pass and (d) with schematic diagram after first stage.

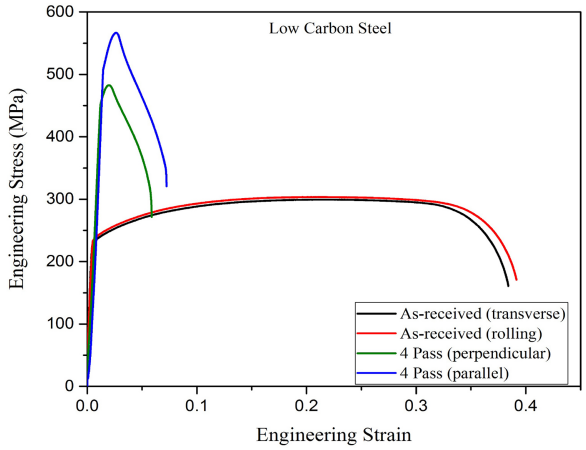

Fig. 7. Engineering stress–strain curves of as-received low carbon steel sheets and after fourth pass.

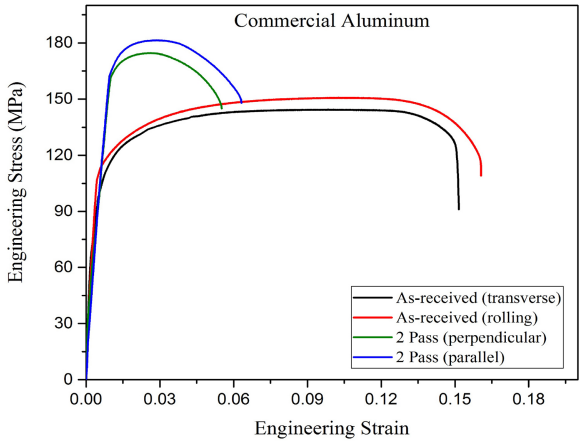

Fig. 8. Engineering stress–strain curves of as-received commercial aluminum sheets and after second pass.

Figs. 7 and 8 represent tensile engineering stress–strain curves of as-received and CGP processed sheet of low carbon steel and commercial aluminum respectively. In general, the rolling direction of sheets is oriented perpendicular to the groove orientation. The CGP pass induces a waviness along the rolling direction due to the periodicity of the grooves, which is reflected in the guage length of the tensile specimen. This introduces local weak spots along the guage length. Many earlier reports [11,12,31] on CGP analyses the tensile behavior post CGP using the samples cut perpendicular to the groove orientations that may have non-uniform thickness in the guage length. To avoid premature localization due to geometric inhomogeneity, it is preferable to test the samples parallel to the groove direction.[1] In the present work, tensile samples were prepared along two orientations, parallel and perpendicular to the grooves. The parallel orientation tensile specimens are uniformly thick in their guage length. The results of low carbon steel and aluminium are shown in Figs. 7 and 8.

[1] Since rolling axis is generally perpendicular to groove orientation, samples parallel to grooves will be along the transverse direction of sheet.

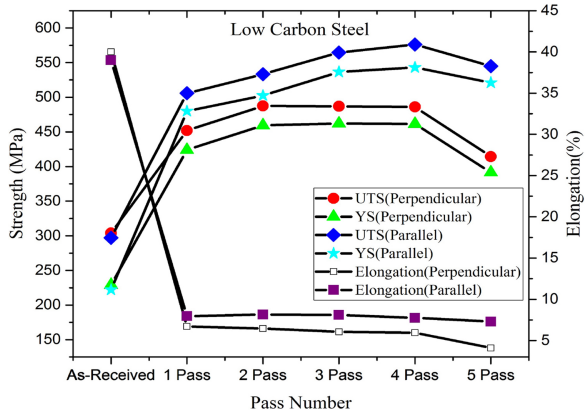

Fig. 9. Variation of tensile properties with pass number in CGP of low carbon steel.

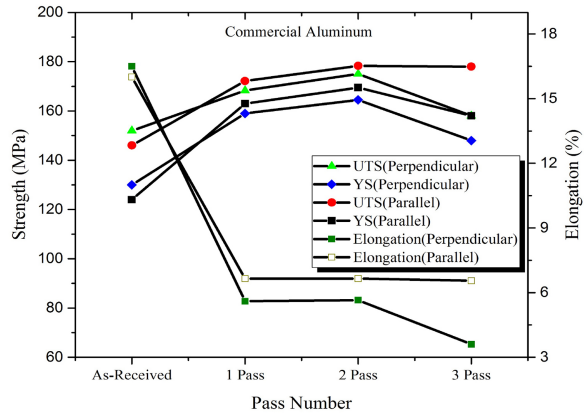

Fig. 10. Variation of tensile properties with pass number in CGP of commercial aluminium.

CGP increased the strength and decreased the elongation as commonly observed earlier [11]. However the shape of the stress–strain curves are distinctly different from each other. In the case of low carbon steel, the instability or maximum stress is achieved at around 3% strain followed by gradual decrease of strength till failure at around 8%. Similarly, the commercially pure aluminium samples maximum stress occurs at around 3% followed by failure at 6%. The post uniform elongation behaviour is unique to the material, the rate of strength decrement in steel is much higher than that observed in aluminium samples. The post uniform elongation is related to the rate dependent behavior of the materials, characterized by strain rate sensitivity. FCC structure in aluminium is less sensitive to rate effects when compared to steels BCC structure.

In both the cases, the ratio of post-uniform elongation to uniform elongation has increased considerably when compared to the as-received condition. The variation of mechanical properties with the number of passes is summarized in Figs. 9 and 10. By the end of fourth pass in low carbon steel, the tensile strength increased from 300 MPa to 576 MPa with the ductility decreasing from 40% to 7.5%. Similarly, the tensile strength and ductility varied from 148 MPa and 16% to 178 MPa and 6.4% respectively in commercially pure aluminium. The CGP process increased the strength by 92% in steel and 20% in aluminium. The difference could be either due to the mechanical properties or number of passes or the combination of both. It can be observed from Figs. 9 and 10 that significant contribution of strength increment is mainly obtained in the first pass. Therefore, the number of passes does not contribute appreciably. The observed difference in strength improvement between aluminium and low carbon steel is due to poor strain hardening capability of commercially pure aluminium, evidenced by the n value (Table 2).

The rate of increment in strength is significant in the first pass followed by gradual decrease till it reaches maximum. The strength eventually drops beyond a certain number of pass. The observation is in line with the reported results in literature [57–59]. The noticeable enhancement in mechanical properties in first pass is attributed to grain refinement and strain hardening by dislocation strengthening due to large plastic strain [60]. In the subsequent passes, the dynamic recovery effect by dislocation annihilation dominates and affects the strength increment [12]. It has been pointed out [21] that the contribution of process induced micro-cracks, in addition to dynamic recovery on the strength reduction at large passes during CGP. Strain hardenability of CGP processed sheet indicated by the strength increment between subsequent passes reduces with increase in number of passes. This is due to the pronounced dislocation multiplication and tangles that reduces the average mean path for dislocation movement during strain hardening [61].

The stress–strain curve of as-received material along rolling and transverse direction indicates that the initial anisotropy is negligible in low carbon steel. In the case of aluminium, strength along rolling direction is higher than that along transverse direction (Figs. 9 and 10). To the reverse, the improvement of strength and reduction of elongation along parallel (to groove) direction is higher than that along perpendicular direction (rolling direction of as-received sheet). This indicates that the reduced strength perpendicular directions is predominantly due to the process induced geometric and strain inhomogeneity rather than initial anisotropy.

The variation of microhardness with passes is measured across the transverse and through thickness direction after CGP processing as illustrated in Fig. 11. The variation with the number of passes (Fig. 12) exhibits a similar trend with strength, as reported in [62]. The proportional increase of strength with hardness is well established in metals. Since the strength obtained at room temperature using CGP is related to the dislocation–dislocation interaction, it is possible to relate the evolution of average dislocation density during CGP process with the hardness.

Due to the complex state of stress during indentation, the hardness measured is influenced by both the statistically stored dislocations (SSD) and the geometrically necessary dislocations (GND). The GNDs during hardness test are generated due to the strain gradient within the substructure. Nix and Gao [63], extended the classical Taylor's dislocation model of flow stress to model the hardness in terms of dislocations is given in Eq. (8). Graça et al. [64] validated their model experimentally using dislocation density measurements from transmission electron microscope (TEM) images.

Using strain gradient plasticity in classical Taylors dislocation model, hardness is directly proportional to square root of dislocation density.

$$HV = 3\sqrt{3}\,\alpha G\, b\sqrt{\rho_t}, \tag{8}$$

where HV is experimental hardness value, α is empirical coefficient (0.3 is taken for this analysis), G is shear modulus (26 GPa for commercial aluminum and 80 GPa for low carbon steel), b is Burgers vector (0.286 nm for aluminum and 0.254 nm for low carbon steel), ρ_t is the dislocation density of deformed region by hardness indention. ρ_t is the given by (Eq. (9))

$$\rho_t = \rho_g + \rho_s \tag{9}$$

where ρ_g and ρ_s respectively refer to GND and SSD.

Following [63], expressions for SSD (ρ_s) and GND (ρ_g) from Vicker's hardness were derived in [65] as given in Eqs. (10 and 11).

$$\rho_s = \frac{HV^2}{27\alpha^2 G^2 b^2} - \rho_g \tag{10}$$

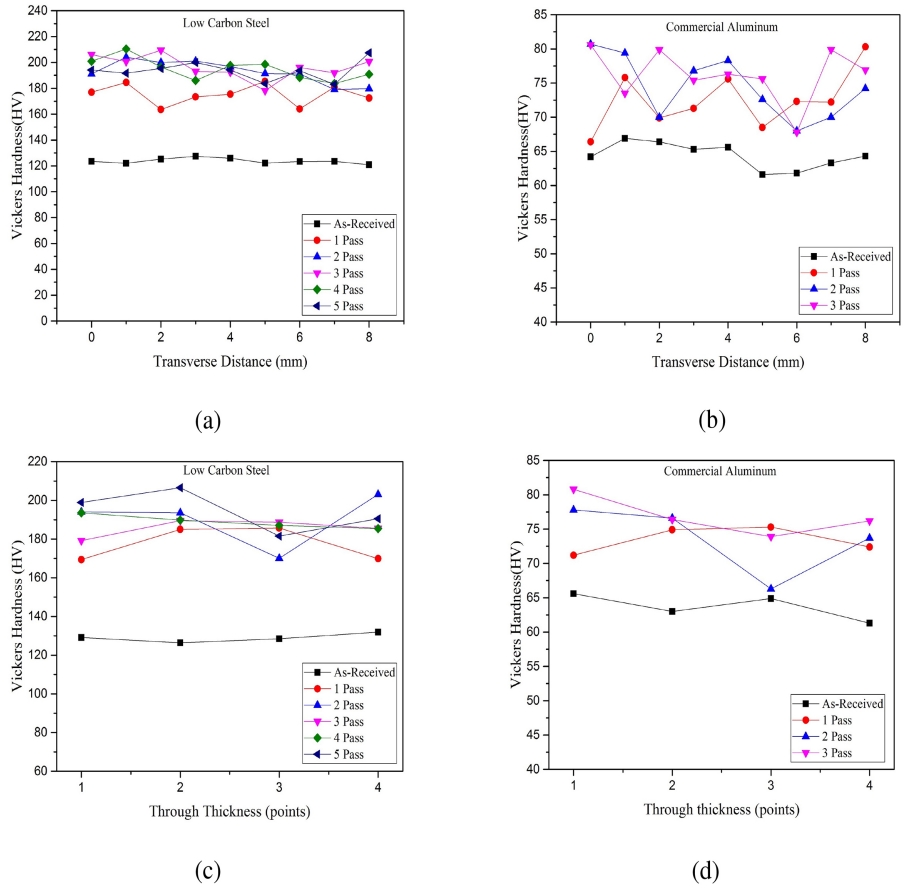

Fig. 11. Hardness distribution in (a) transverse direction of low carbon steel, (b) transverse of commercial aluminum, (c) through thickness direction of low carbon steel and (d) through thickness direction of commercial aluminum.

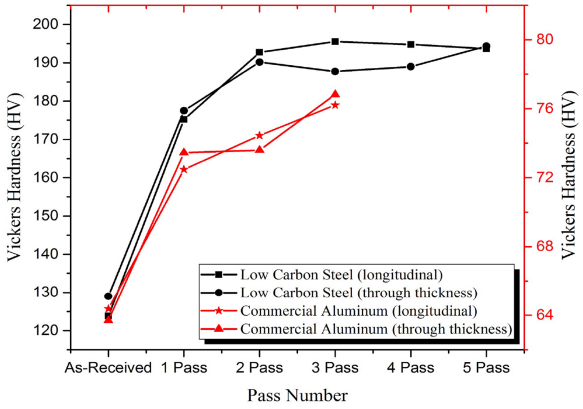

Fig. 12. Variation of average hardness value with pass number in transverse and through thickness directions of low carbon steel and commercial aluminum.

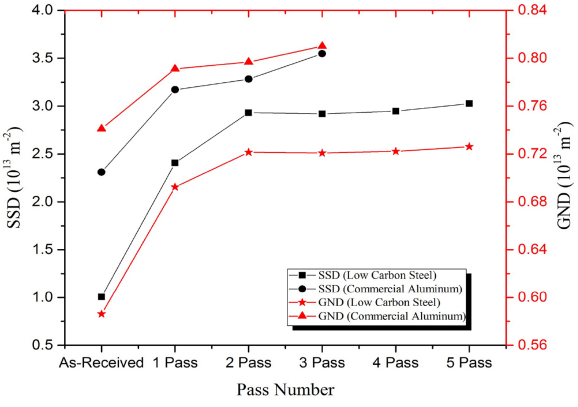

Fig. 13. Variation of statically stored dislocation (SSD) density and geometrically necessary dislocation (GND) density with pass number in low carbon steel and commercial aluminum.

$$\rho_g = \frac{3\sqrt{2}\sqrt{\mathrm{HV}}\cot\theta}{\sqrt{1.72}\pi^2 b\sqrt{F}} \tag{11}$$

where θ is Vickers indenter semi-angle (68°) and F is load applied (25 g for commercial aluminum and 100 g for low carbon steel material).

Fig. 13 shows the variation of dislocation density with the number of passes which is similar to the trend of hardness. Initially, the amount of dislocations (SSD and GND) are less in both as received materials. The rate of dislocation generation is high during the first pass and gradually decrease in the subsequent passes. It also shows that the rate of dislocation generation in low carbon steel is more compared to commercial aluminum. Fig. 14 illustrates the ratio of SSD and GND with the number of passes in two materials. SSD/GND ratio is a measure of strain gradient present within the material. The ratio of aluminum is always higher than low carbon steel, indicating strong strain gradient in the former. The number of passes to failure is less in aluminium due to the localization caused by strong strain gradient. It is also observed that the first pass witnessed a steep change in the SSD/GND in low carbon steel when compared to aluminium. The change in the ratio is not significant in the subsequent passes. This indicates that the

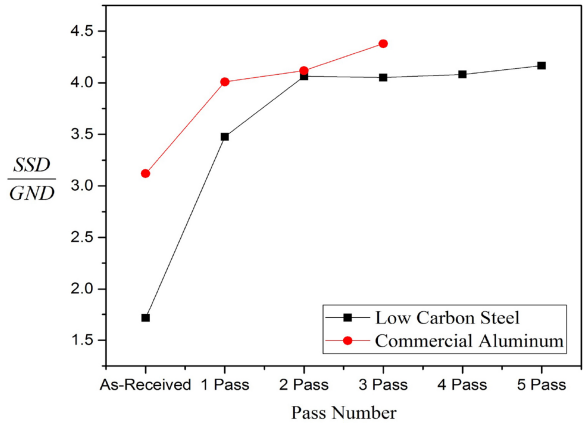

Fig. 14. Variation of ratio of statically stored dislocation (SSD) density and geometrically necessary dislocation (GND) density with pass number in low carbon steel and commercial aluminum.

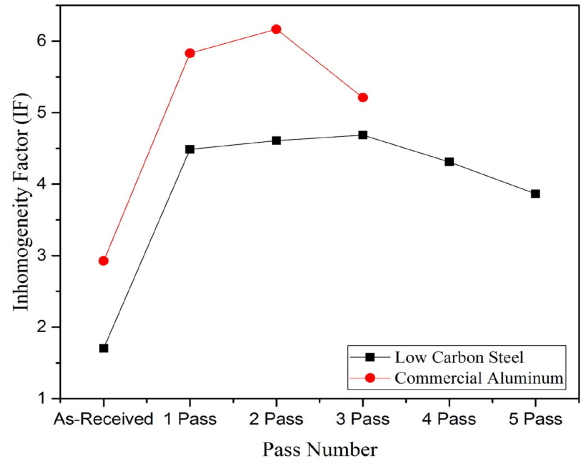

Fig. 15. Inhomogeneity factor variation with pass number for low carbon steel and commercial aluminum.

Table 4
Parameters incorporated in benchmark simulations.

Input parameter	Copper	Nickel	Aluminum
Sheet size (mm × mm)	80 × 5	30 × 2	130 × 5
Friction coefficient	0.1	0.1	0
Number of elements	1600	960	2600

multiplication of SSD is primarily in the first pass. High GND in aluminium obstruct the multiplication of SSD leading to less increment in strength.

The hardness distribution along transverse and through thickness direction on different passes of both materials are shown in Fig. 12. Using Eq. (12), inhomogeneity factor (IF) is used to quantify the non-uniformity in hardness distribution.

$$\text{Inhomogeneity factor (IF)} = \frac{\sqrt{\sum_{i=1}^{n}(H_i - H_{\text{avg}})^2/(n-1)}}{H_{\text{avg}}} \times 100 \quad (12)$$

where H_i is hardness value at i-th point, H_{avg} is average hardness value, and n is number of measurements in single sample.

Larger IF value indicates more inhomogeneity in material properties. Fig. 15 shows that IF value increases in first two passes and it is either consistent or decreases slightly in remaining passes. IF is more in commercial aluminum compared to low carbon steel material. It is interesting to note that SSD/GND ratio correlates with the above discussion on IF. It can be directly concluded that the inhomogeneity is related to the accumulation of GND in the material, which retards the strain hardening capability leading to localization and failure.

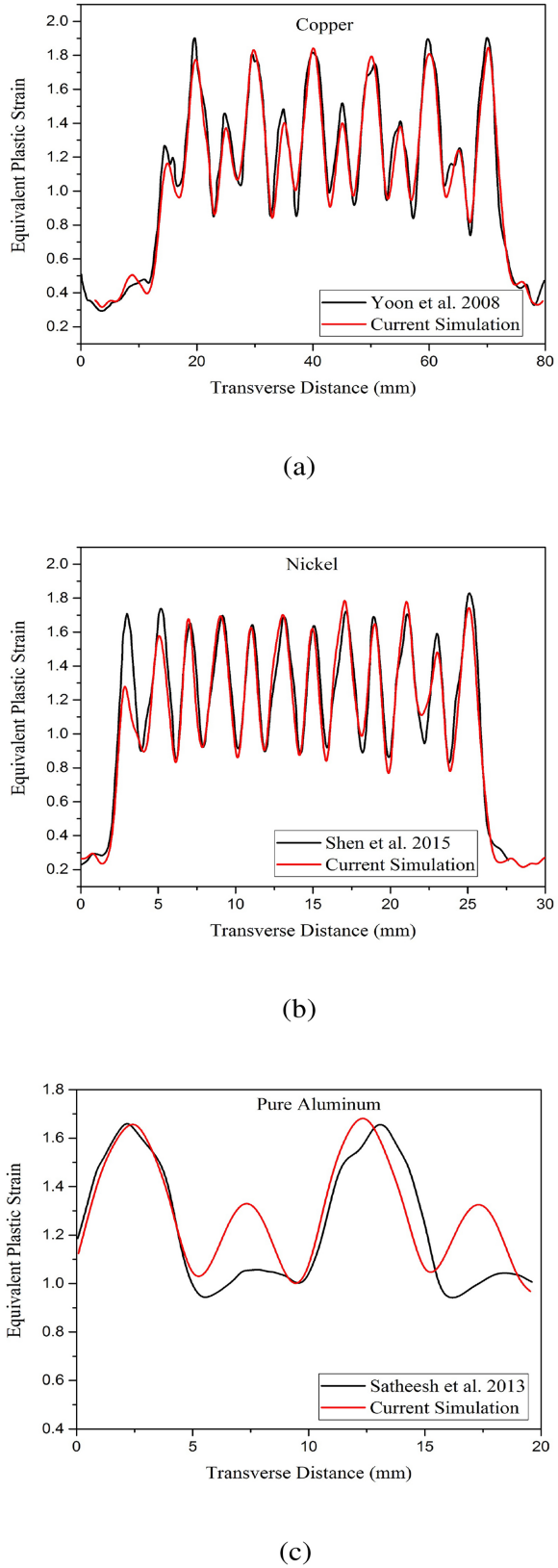

Fig. 16. Comparison of equivalent plastic strain distribution after first pass from literature with current simulation for (a) copper [20], (b) nickel [31] and (c) aluminum [30].

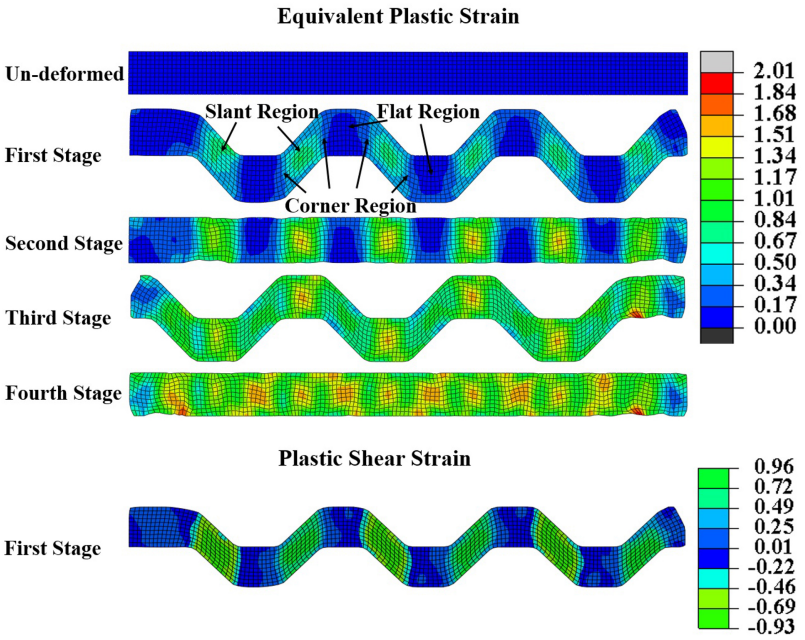

Fig. 17. Equivalent plastic strain distribution contours after each stage and plastic shear strain after first stage of low carbon steel.

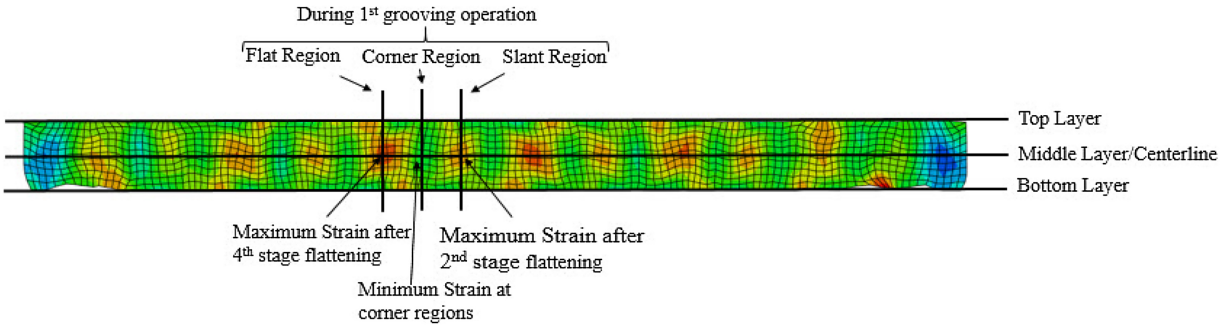

Fig. 18. Representation of different regions after fourth stage of CGP process simulation of low carbon steel.

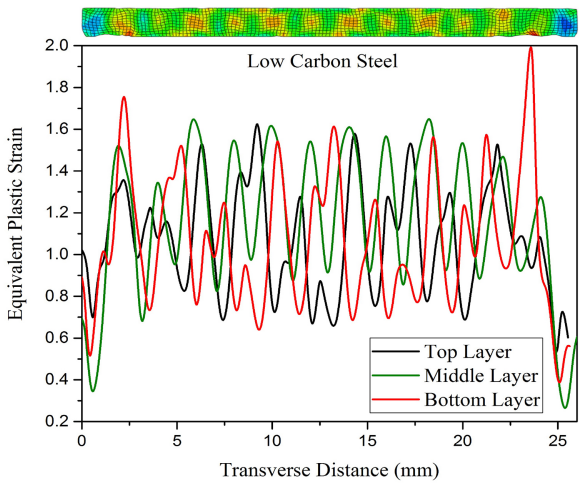

Fig. 19. Strain distributions of low carbon steel in transverse direction in three different layers after first pass.

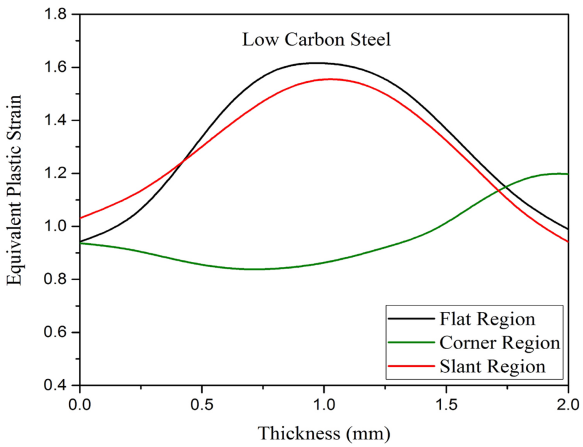

Fig. 20. Strain distributions of low carbon steel in through thickness direction in three different regions after first pass.

4.3. Validation of finite element model

Finite element model and simulations were performed following the description in Section 3. To evaluate the finite element model including mesh, constraints and boundary conditions, simulations were initially performed to benchmark the results against that published earlier. The simulation results on copper by [20], nickel by [31] and aluminum by [30] were chosen for the study. The simulations were repeated using the material properties, constraints and boundary conditions defined in the respective literature. The sheet (Table 4) was meshed using element size of 0.25 mm × 0.25 mm by CPE4R (A 4-node bilinear plane strain

Table 5
Average equivalent strain values in transverse directions for low carbon steel, commercial aluminum and AA5083 after first pass.

Material	Low carbon steel	Commercial aluminum	AA5083
Top layer	1.09	1.07	1.02
Middle layer	1.22	1.21	1.18
Bottom layer	1.11	1.10	1.06

Table 6
Average equivalent strain values in through thickness direction for low carbon steel, commercial aluminum and AA5083 after first pass.

Material	Low carbon steel	Commercial aluminum	AA5083
Flat region	1.31	1.28	1.38
Corner region	0.97	0.97	0.92
Slant region	1.28	1.28	1.2

quadrilateral, reduced integration, hourglass control) element type. All the cases involve only isotropic hardening on following literature.

The equivalent strain predicted in the present work using the data from literature is compared with the results published, as shown in Fig. 16. A good correlation is obtained between the present work and the results in literature. Therefore, the finite element model is considered valid for performing simulations in low carbon steel and Aluminium. In the present work, both isotropic and combined hardening are considered for simulation.

Equivalent strain distributions of repeated simulations in this study and available simulations in the literature are compared and validated using isotropic hardening model. Using the same techniques, isotropic and combined (isotropic and kinematic) hardening model were implemented on low carbon steel, commercial aluminum and AA5083 materials in the current study.

Die geometry with sheet from literature was simulated using respective three material properties (stress–strain curve) up to one pass of CGP process.

4.4. Strain distributions using isotropic hardening model

Fig. 17 shows the contour of equivalent plastic strain and plastic shear strain distributions of CGP process of low carbon steel. It is observed that equivalent plastic strain and plastic shear strain contours are similar to each other in the first stage. Further analysis is on the basis of equivalent plastic strain instead of plastic shear strain due to reverse strain path and additional deformation of bending and stretching. Strain distribution contours of the three materials are similar. The equivalent plastic strain distributions along the transverse and through thickness direction for low carbon steel material after the fourth stage are shown in Figs. 19 and 20. The strain distribution is non-homogeneous along the transverse and through thickness direction. The non-homogeneity along the transverse direction is evident from Fig. 19 where the variation of equivalent strain in three sections, top, middle and bottom layers parallel to the transverse direction is shown. In addition to that, the geometric die features also introduces inhomogeneity. The through thickness variation in selected regions such as corner, flat and slant region in Fig. 20 quantifies the inhomogeneity. Fig. 18 represents the different regions after fourth stage of CGP process simulation of low carbon steel. Unlike the theoretical estimate of 1.16 uniform plastic strain distribution at the end of one pass, non-uniform strain distribution is observed throughout the sheet. As mentioned earlier, inhomogeneous strain distribution result in non-uniform grain refinement. All transverse and through thickness layers demonstrate the variation of equivalent plastic strain after first pass. Only the results of low carbon steel is shown, although similar behaviour was observed in other materials. The strain distribution in middle layer varies

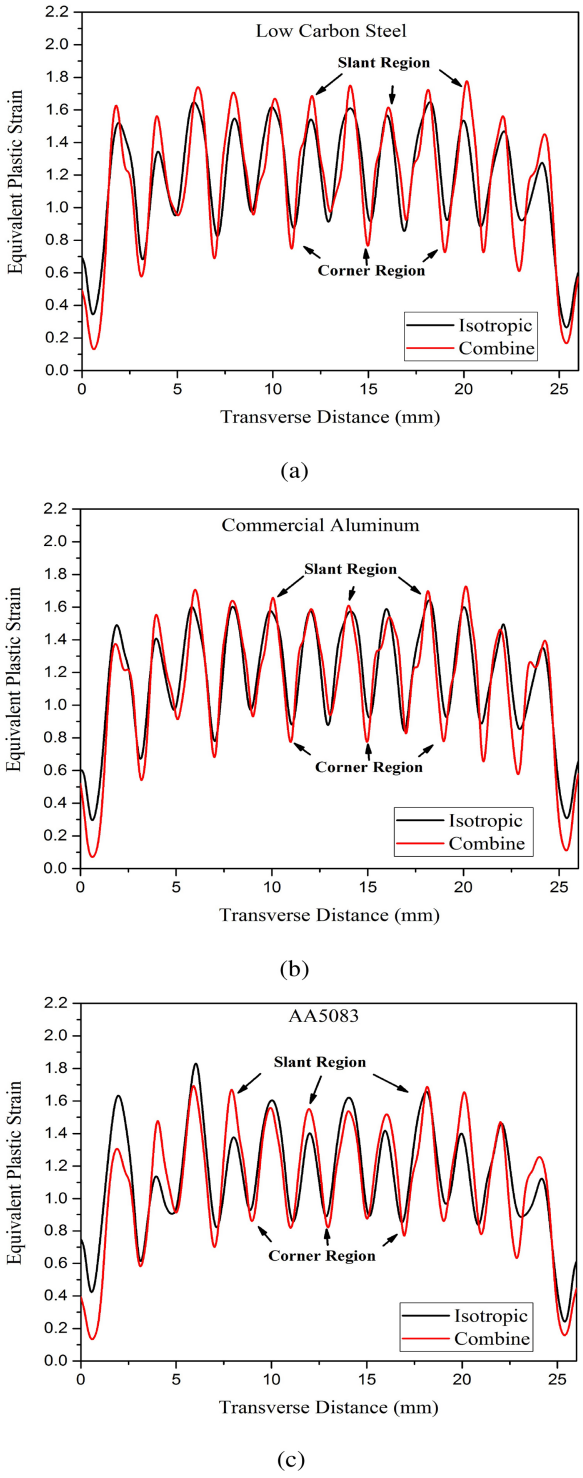

Fig. 21. Comparison of strain distribution in transverse direction of (a) low carbon steel, (b) commercial aluminum and (c) AA5083 materials using isotropic and combined hardening model after first pass.

harmonically and almost symmetrically distributed after each groove. Fig. 20 shows that the strain at the center of flat and slant regions are more compared to corner regions (interface of flat and slant regions) and decrease toward sheet surface and corner interface. This is due to the additional bending at the corner regions [20]. The center of slant region is subjected to large shear deformation. A similar trend of effective strain distribution in finite element simulation of CGP process is also observed in [30].

Table 7
Comparison of maximum equivalent strain, average equivalent strain and inhomogeneity factor values from simulation after first pass using isotropic and combined hardening models.

Material	Isotropic hardening			Combined hardening		
	Maximum equivalent strain	Average equivalent strain	Inhomogeneity factor	Maximum equivalent strain	Average equivalent strain	Inhomogeneity factor
Low carbon steel	1.64	1.22	23.4	1.80	1.21	29.2
Commercial aluminum	1.62	1.21	23.7	1.75	1.18	28.7
AA5083	1.70	1.18	24.7	1.73	1.15	28.0

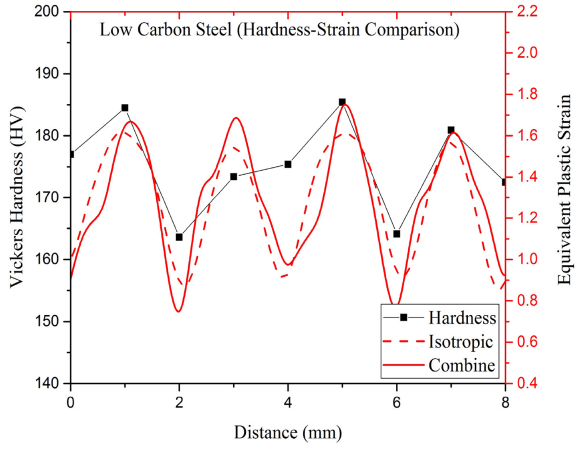

(a)

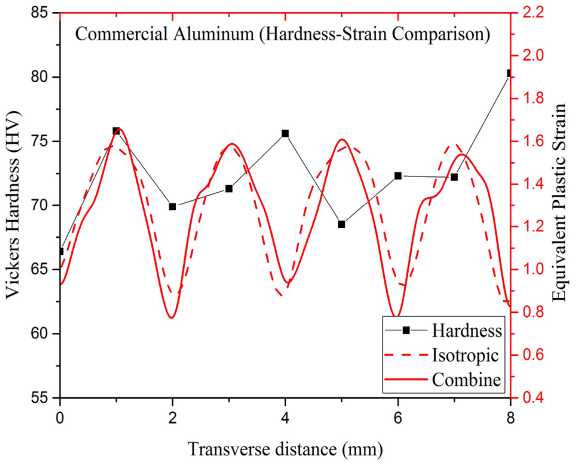

(b)

Fig. 22. Comparison of strain distribution in transverse direction with hardness of (a) low carbon steel and (b) commercial aluminum using isotropic and combined hardening model after first pass.

This strain inhomogeneity leads to non-uniform distribution of strength and hardness [66].

Tables 5 and 6 show the average values of effective plastic strain along different layers in transverse and through thickness directions. It is observed that average plastic strain values at top and bottom layers are less compared to middle layer of the sheet in all the three materials. The average values from three horizontal layers for commercial aluminum, low carbon steel and AA5083 are 1.14, 1.13 and 1.09 respectively. Average values are quite close to 1.16 (theoretical calculated value). Similarly, flat and slant regions show high average plastic strain values compared to corner regions in through thickness direction of all three materials.

4.5. Finite element simulation using combined hardening model

The loading of first stage of the first pass is proportional and the isotropic hardening assumption is valid. As discussed, consideration of Bauschinger effect assumes importance beyond second stage. Fig. 21 compares the equivalent strain distribution of the three materials considered in the present work assuming isotropic and combined hardening behaviour. Table 7 compares values of maximum equivalent strain, average equivalent strain and inhomogeneity factor of strain distribution from simulations using isotropic and combined hardening model. The maximum equivalent strain values are estimated by averaging the four peak strain values in each material. The maximum equivalent strain and strain inhomogeneity factor are distinctly higher when combined hardening models are assumed. The trend of hardness distribution in the plane of the sheet can be correlated with the equivalent strain [30]. Since the trend of both isotropic and combined hardening are similar, no specific conclusions can be drawn from this comparison (Fig. 22) except slight difference in strain at slant and corner regions. Strains are distinctly higher at the slant regions and lower at the corner regions when using combine hardening model for simulation. Shear and reverse shear deformation in successive stages leads to higher strain at the slant region. Similarly, corner region shows lower strain because it involves additional bending instead of pure shear deformation (Fig. 6(d)). Since the maximum strain can be correlated with the strain localization leading to failure, the improved prediction considering Bauschinger effect is expected to correlate well with the experimental failure.

Similar to the IF (Eq. (12)), a strain based inhomogeneity factor can be described as

$$\text{Inhomogeneity factor (IF)} = \frac{\sqrt{\sum_{i=1}^{n}(S_i - S_{\text{avg}})^2/(n-1)}}{S_{\text{avg}}} \times 100 \quad (13)$$

where S_i is equivalent strain at i-th point, S_{avg} is average equivalent strain value, and n is number of measurements in single sample.

This strain based IF as given in Eq. (13) is used to quantify the non-uniformity in strain distribution. Inhomogeneity of strain distribution in three materials of combined hardening model is higher than the isotropic hardening model. As indicated earlier, inhomogeneity of strain distribution results in non-uniformity of ultrafine grains and mechanical properties. Combined hardening model predicts higher inhomogeneity and non-uniformity of grain distribution than the isotropic hardening model. Further studies are planned in future to correlate the micro structure evolution during CGP stages to verify the accuracy of hardening models.

5. Conclusions

Constrained groove pressing of low carbon steel, commercial aluminum and AA5083 alloy was investigated using experimental and numerical techniques. The specific findings are summarized as follows:

1 Low carbon steel and commercial aluminum materials were successfully processed for five passes (plastic strain 5.8) and three

passes with (plastic strain 3.48) respectively. The strength increment is related to the strain hardening capability of the material. Despite high n value, AA5083 alloy failed in the first pass and it possibly could be due to the solute-dislocation interaction in the alloy with lesser stacking fault energy.

2 The ratio of statistically stored dislocation (SSD) with geometrically necessary dislocations (GND) correlates well with the inhomogeneity factor estimated from hardness. Based on the trend, it is inferred that the sluggish increment in strength in aluminium during CGP is due to high value of SSD/GND.

3 Finite element simulation of CGP was validated with the results in literature. Most of the existing studies assume isotropic hardening that cannot account for the Bauschinger effect in CGP. The present work compared the predictions using isotropic hardening and combined isotropic-kinematic hardening. The peak strain and strain based inhomogeneity factor predicted assuming combined hardening models were higher than that of isotropic hardening.

4 Strength and hardness increased with increase in number of passes. Strength of the sheet improved by 92% in low carbon steel after fourth pass and 20% in commercial aluminum after second pass. The tensile strength, yield strength and elongation in parallel to grooves are higher than that along perpendicular direction. Inhomogeneity in hardness distribution is observed in the processed sheet along transverse and through thickness directions due to non-uniform distribution of strain.

Acknowledgment

This research work was supported by the grant received from Department of Science and Technology (DST) India, vide project no. YSS/2015/001342. Authors would like to thank Dr. Kanwer Singh Arora of Tata Steel R&D for his assistance in cyclic testing.

References

[1] Valiev R. Nanostructuring of metals by severe plastic deformation for advanced properties. Nat Mater 2004;3(8):511–6.
[2] Segal V. Severe plastic deformation: simple shear versus pure shear. Mater Sci Eng A 2002;338(1):331–44.
[3] Segal V. Materials processing by simple shear. Mater Sci Eng A 1995;197(2):157–64.
[4] Zhilyaev AP, Langdon TG. Using high-pressure torsion for metal processing: fundamentals and applications. Prog Mater Sci 2008;53(6):893–979.
[5] Huang J, Zhu Y, Jiang H, Lowe T. Microstructures and dislocation configurations in nanostructured Cu processed by repetitive corrugation and straightening. Acta Mater 2001;49(9):1497–505.
[6] Cherukuri B, Srinivasan R. Properties of AA6061 processed by multi-axial compressions/forging (MAC/F). Mater Manuf Process 2006;21(5):519–25.
[7] Cui Q, Ohori K. Grain refinement of high purity aluminium by asymmetric rolling. Mater Sci Technol 2000;16(10):1095–101.
[8] Saito Y, Utsunomiya H, Tsuji N, Sakai T. Novel ultra-high straining process for bulk materials-development of the accumulative roll-bonding (ARB) process. Acta Mater 1999;47(2):579–83.
[9] Beygelzimer Y, Varyukhin V, Synkov S, Orlov D. Useful properties of twist extrusion. Mater Sci Eng A 2009;503(1):14–7.
[10] Shin DH, Park JJ, Kim YS, Park KT. Constrained groove pressing and its application to grain refinement of aluminum. Mater Sci Eng A 2002;328(1):98–103.
[11] Khodabakhshi F, Kazeminezhad M, Kokabi A. Constrained groove pressing of low carbon steel: nano-structure and mechanical properties. Mater Sci Eng A 2010;527(16):4043–9.
[12] Kumar SS, Raghu T. Structural and mechanical behaviour of severe plastically deformed high purity aluminium sheets processed by constrained groove pressing technique. Mater Des 2014;57:114–20.
[13] Khorrami MS, Kazeminezhad M, Kokabi A. Thermal stability of aluminum after friction stir processing with SiC nanoparticles. Materials Des 2015;80:41–50.
[14] Kumar G, Niranjan GG, Uday C. Grain refinement in commercial purity titanium sheets by constrained groove pressing. Materials science forum, vol. 683. 2011. p. 233–42.
[15] Thirugnanam A, Kumar TS, Chakkingal U. Tailoring the bioactivity of commercially pure titanium by grain refinement using groove pressing. Mater Sci Eng C 2010;30(1):203–8.
[16] Peng K, Su L, Shaw LL, Qian KW. Grain refinement and crack prevention in constrained groove pressing of two-phase Cu-Zn alloys. Scrip Mater 2007;56(11):987–90.
[17] Meyers MA, Mishra A, Benson DJ. Mechanical properties of nanocrystalline materials. Prog Mater Sci 2006;51(4):427–556.
[18] Humphreys FJ, Hatherly M. Recrystallization and related annealing phenomena. Elsevier; 2012.
[19] Parvin H, Kazeminezhad M. Development a dislocation density based model considering the effect of stacking fault energy: severe plastic deformation. Comput Mater Sci 2014;95:250–5.
[20] Yoon SC, Krishnaiah A, Chakkingal U, Kim HS. Severe plastic deformation and strain localization in groove pressing. Comput Mater Sci 2008;43(4):641–5.
[21] Krishnaiah A, Chakkingal U, Venugopal P. Production of ultrafine grain sizes in aluminium sheets by severe plastic deformation using the technique of groove pressing. Scrip Mater 2005;52(12):1229–33.
[22] Krishnaiah A, Chakkingal U, Venugopal P. Applicability of the groove pressing technique for grain refinement in commercial purity copper. Mater Sci Eng A 2005;410:337–40.
[23] Sajadi A, Ebrahimi M, Djavanroodi F. Experimental and numerical investigation of Al properties fabricated by CGP process. Mater Sci Eng A 2012;552:97–103.
[24] Wang Z, Liang P, Guan Y, Liu Y, Jiang L. Experimental investigation of pure aluminum sheets processed by constrained groove pressing. Indian J Eng Mater Sci 2014;21(2):121–7.
[25] Peng K, Zhang Y, Shaw LL, Qian KW. Microstructure dependence of a Cu-38Zn alloy on processing conditions of constrained groove pressing. Acta Mater 2009;57(18):5543–53.
[26] Gupta AK, Maddukuri TS, Singh SK. Constrained groove pressing for sheet metal processing. Prog Mater Sci 2016;84:403–62.
[27] Jiang Z, Zhao J, Lu H, Wei D, Manabe K, Zhao X, et al. Influences of temperature and grain size on the material deformability in microforming process. Int J Mater Form 2017;10(5):753–64.
[28] Li J, Xu J, Wang CT, Shan D, Guo B, Langdon TG. Microstructural evolution and micro-compression in high-purity copper processed by high-pressure torsion. Adv Eng Mater 2016;18(2):241–50.
[29] Yadav PC, Sinhal A, Sahu S, Roy A, Shekhar S. Microstructural inhomogeneity in constrained groove pressed Cu-Zn alloy sheet. J Mater Eng Perform 2016;25(7):2604–14.
[30] Satheesh Kumar S, Balasundar I, Raghu T. Finite element analysis of constrained groove pressing of pure aluminum sheets. Int J Comput Mater Sci Eng 2013;2(01):1350001.
[31] Wang ZS, Guan YJ, Wang GC, Zhong CK. Influences of die structure on constrained groove pressing of commercially pure Ni sheets. J Mater Process Technol 2015;215:205–18.
[32] Abel A, Muir H. The Bauschinger effect and stacking fault energy. Philos Mag 1973;27(3):585–94. https://doi.org/10.1080/14786437308219233.
[33] Watson J, Brown G. Torsional prestrain and the Bauschinger effect in steel. Scrip Metall 1973;7(1):739–43. https://doi.org/10.1016/0036-9748(73)90125-7.
[34] Boger RK, Wagoner RH, Barlat F, Lee MG, Chung K. Continuous, large strain, tension/compression testing of sheet material. Int J Plasticity 2005;21(12):2319–43. https://doi.org/10.1016/j.ijplas.2004.12.002.
[35] Weiss M, Kupke A, Manach P, Galdos L, Hodgson P. On the Bauschinger effect in dual phase steel at high levels of strain. Mater Sci Eng A 2015;643:127–36. https://doi.org/10.1016/j.msea.2015.07.037.
[36] Naseri M, Reihanian M, Borhani E. Effect of strain path on microstructure, deformation texture and mechanical properties of nano/ultrafine grained AA1050 processed by accumulative roll bonding (ARB). Mater Sci Eng A 2016;673:288–98.
[37] Kumar SS, Raghu T. Strain path effects on microstructural evolution and mechanical behaviour of constrained groove pressed aluminium sheets. Mater Des 2015;88:799–809.
[38] Abel A, Muir H. The Bauschinger effect and discontinuous yielding. Philo Mag 1972;26(2):37–41. https://doi.org/10.1080/14786437208227444.
[39] Wang Y, Tomota Y, Harjo S, Gong W, Ohmura T. In-situ neutron diffraction during tension-compression cyclic deformation of a pearlite steel. Mater Sci Eng A 2016;676:522–30. https://doi.org/10.1016/j.msea.2016.08.122.
[40] Saleh AA, Clausen B, Brown DW, Pereloma EV, Davies CHJ, Tomé CN, et al. On the feasibility of partial slip reversal and de-twinning during the cyclic loading of TWIP steel. Mater Lett 2016;182:294–7. https://doi.org/10.1016/j.matlet.2016.07.005.
[41] Hu J, Chen B, Smith DJ, Flewitt PE, Cocks AC. On the evaluation of the Bauschinger effect in an austenitic stainless steel? The role of multi-scale residual stresses. Int J Plasticity 2016;84:203–23. https://doi.org/10.1016/j.ijplas.2016.05.009.
[42] Prager W. A new methods of analyzing stresses and strains in work hardening plastic solids. J Appl Mech (ASME) 1956;23:493–6.
[43] Chaboche JL. Time-independent constitutive theories for cyclic plasticity. Int J Plasticity 1986;2(2):149–88.
[44] Cao J, Lee W, Cheng HS, Seniw M, Wang HP, Chung K. Experimental and numerical investigation of combined isotropic-kinematic hardening behavior of sheet metals. Int J Plasticity 2009;25(5):942–72. https://doi.org/10.1016/J.IJPLAS.2008.04.007.
[45] Zhou C, Chen Z, Lee J, Lee M, Wagoner R. Implementation and application of a temperature-dependent Chaboche model. Int J Plasticity 2015;75:121–40. https://doi.org/10.1016/j.ijplas.2015.03.002.
[46] Khademi E, Majzoobi GH, Bonora N, Gentile D. Experimental modeling of strain-dependent cyclic plasticity for prediction of hysteresis curve. J Strain Anal Eng Des 2015;50(5):314–24. https://doi.org/10.1177/0309324715581953.
[47] Chung K, Lee M-G, Kim D, Kim C, Wenner ML, Barlat F. Spring-back evaluation of automotive sheets based on isotropic-kinematic hardening laws and non-quadratic anisotropic yield functions: Part I: Theory and formulation. Int J Plasticity 2005;21(5):883–914. https://doi.org/10.1016/j.ijplas.2004.05.015.
[48] Liao J, Xue X, Lee MG, Pereira AB. Constitutive modeling for path-dependent behavior and its influence on twist springback. Int J Plasticity 2017;93:64–88. https://

doi.org/10.1016/J.IJPLAS.2017.02.009.
[49] Dafalias YF, Popov EP. Plastic internal variables formalism of cyclic plasticity. J Appl Mech 1976;43(4):645–51.
[50] Lee MG, Kim D, Kim C, Wenner ML, Wagoner RH, Chung K. A practical two-surface plasticity model and its application to spring-back prediction. Int J Plasticity 2007;23(7):1189–212. https://doi.org/10.1016/j.ijplas.2006.10.011.
[51] Yoshida F, Uemori T. A model of large-strain cyclic plasticity describing the Bauschinger effect and workhardening stagnation. Int J Plasticity 2002;18(5):661–86. https://doi.org/10.1016/S0749-6419(01)00050-X.
[52] Nguyen NT, Lee MG, Kim JH, Kim HY. A practical constitutive model for AZ31B Mg alloy sheets with unusual stress-strain response. Finite Elem Anal Des 2013;76:39–49. https://doi.org/10.1016/j.finel.2013.08.008.
[53] E8/E8M-16a A. Standard test methods for tension testing of metallic materials. Tech. Rep. West Conshohocken, PA: ASTM International; 2016.
[54] E606-92(2004)e1 A. Standard practice for strain-controlled fatigue testing. Tech. Rep. West Conshohocken, PA: ASTM International; 2004.
[55] Armstrong PJ. A mathematical representation of the multiaxial Bauschinger effect. CEBG Report RD/B/N, 731 1966.
[56] Bari S, Hassan T. Anatomy of coupled constitutive models for ratcheting simulation. Int J Plasticity 2000;16(3):381–409.
[57] Valiev RZ, Langdon TG. Principles of equal-channel angular pressing as a processing tool for grain refinement. Prog Mater Sci 2006;51(7):881–981.
[58] Eizadjou M, Manesh HD, Janghorban K. Microstructure and mechanical properties of ultra-fine grains (UFGs) aluminum strips produced by ARB process. J Alloys Compd 2009;474(1):406–15.
[59] Gashti S, Fattah-Alhosseini A, Mazaheri Y, Keshavarz M. Effects of grain size and dislocation density on strain hardening behavior of ultrafine grained AA1050 processed by accumulative roll bonding. J Alloys Compd 2016;658:854–61.
[60] Langdon TG. The principles of grain refinement in equal-channel angular pressing. Mater Sci Eng A 2007;462(1):3–11.
[61] Wang Y, Ma E. Strain hardening, strain rate sensitivity, and ductility of nanostructured metals. Mater Sci Eng A 2004;375:46–52.
[62] Khodabakhshi F, Haghshenas M, Eskandari H, Koohbor B. Hardness–strength relationships in fine and ultra-fine grained metals processed through constrained groove pressing. Mater Sci Eng A 2015;636:331–9.
[63] Nix WD, Gao H. Indentation size effects in crystalline materials: a law for strain gradient plasticity. J Mech Phys Solids 1998;46(3):411–25.
[64] Graça S, Colaço R, Carvalho P, Vilar R. Determination of dislocation density from hardness measurements in metals. Mater Lett 2008;62(23):3812–4.
[65] Nazari A, Mohandesi JA, Tavareh S. Microhardness profile prediction of a graded steel by strain gradient plasticity theory. Comput Mater Sci 2011;50(5):1781–4.
[66] Peng K, Mou X, Zeng J, Shaw LL, Qian KW. Equivalent strain, microstructure and hardness of H62 brass deformed by constrained groove pressing. Comput Mater Sci 2011;50(4):1526–32.